Chapter 1
Soft X-ray Tomography Imaging for Biological Samples

J. Otón, C.O.S. Sorzano, F.J. Chichón, J.L. Carrascosa, J.M. Carazo and R. Marabini

Abstract *Soft X-ray Tomographic* (TomoX) microscopy is becoming a valuable technique for the analysis of the organization of cellular structures, filling a resolution gap between electron and confocal microscopy. TomoX is based on the possibility of imaging three-dimensional fully hydrated cells under cryo conditions without any chemical pre-treatment using soft X-rays. Unfortunately, from an image formation point of view, TomoX projections suffers from inaccuracies due to the limited depth of field (DOF) of the objective lens. Thus, modeling the image formation process is decisive to understanding how TomoX projections are formed and to mitigating the effect of these DOF inaccuracies. A review of the state of the art regarding image modeling is presented in this chapter.

1.1 Introduction

One of the most recent tools used to understand the mechanisms that take place within the cell is *Cellular soft X-ray Tomography* (TomoX) (Schneider, 1998). This technique is able to visualize whole cells in cryo conditions with a resolution be-

J. Otón, C.O.S. Sorzano, F.J. Chichón, J.L. Carrascosa, J. M. Carazo
Biocomputing Unit, National Center for Biotechnology (CSIC), c/Darwin, 3, Campus Universidad Autónoma, 28049 Cantoblanco, Madrid, Spain, e-mail: joton@cnb.csic.es

C.O.S. Sorzano
Bioengineering Lab., Universidad CEU San Pablo, Campus Urb. Montepríncipe s/n, 28668 Boadilla del Monte, Madrid, Spain

R. Marabini
Escuela Politécnica Superior, Universidad Autónoma de Madrid, Campus Universidad Autónoma, 28049 Cantoblanco, Madrid, Spain

J.L. Carrascosa
Instituto Madrileo de Estudios Avanzados en Nanociencia (IMDEA Nanociencia), Cantoblanco, Madrid, Spain

tween 50 and 10 nm (Rehbein et al, 2009). Many studies have presented 3D reconstructions generated by X-ray microscopy (Weiss et al, 2000; Thieme et al, 2003; Larabell, 2004; Gros et al, 2005; Gu et al, 2007; Parkinson and McDermott, 2008; Uchida et al, 2009; Carrascosa et al, 2009; Hanssen and Knoechel, 2012; McDermott et al, 2012; Chichón et al, 2012).

Usually, tomograms are reconstructed by processing the data using software developed for electron microscopy (EM) data (as can be SPIDER (Frank et al, 1996), BSOFT (Heymann et al, 2008), IMOD (Kremer et al, 1996) or XMIPP (Sorzano et al, 2004)). Because the reconstruction algorithms in these packages do not take into account the specific features of image formation in TomoX, the obtained results are not as optimal as if the reconstruction process were tuned to compensate for the effects of the microscope optical system. In this chapter, we introduce an image formation model under an incoherent illumination condition. Moreover, we analyze the effects of the image formation process into reconstructed data as a first step toward the development of specific reconstruction algorithms.

1.2 Interaction of soft X-rays with matter

There are different ways X-rays interact with matter, namely, absorption, elastic scattering and inelastic scattering (or Compton scattering). In the case of soft X-rays (from approximately 250 eV to several thousand eV (Attwood, 2007)), because the cross section for elastic scattering is a factor of 10^3–10^4 smaller than the photoelectric effect and because inelastic scattering is basically negligible, the dominant effect is the photoelectric absorption (Kirz et al, 1995).

To describe the interaction of matter with X-ray radiation, we suppose a nonmagnetic medium, where the complex refractive index $\tilde{n}$ relates to the complex scattering factor $\tilde{f} = f_1 + \mathrm{i}f_2$ as

$$\tilde{n} = 1 - \frac{n_a r_e \lambda^2}{2\pi}(f_1 + \mathrm{i}f_2), \tag{1.1}$$

where n_a is the number of atoms per unit volume, r_e is the classical electron radius and λ is the illumination wavelength (Kirz et al, 1995).

Because the complex refractive index can be also defined in terms of absorption and phase shift as $\tilde{n} = 1 - \delta - \mathrm{i}\beta$, the electric field of a plane wave along the medium is:

$$\begin{aligned} U(x,y,z) &= U_{0,0}(x,y)\exp(-\mathrm{i}k\tilde{n}z) \\ &= U_{0,0}(x,y)\exp(-\mathrm{i}kz)\exp(\mathrm{i}k\delta z)\exp(-k\beta z) \\ &= U_0(x,y,z)\exp(-\mathrm{i}kz), \end{aligned} \tag{1.2}$$

where $U_{0,0}(x,y)$ is the field amplitude for the reference plane $z=0$, $\mathrm{i}=\sqrt{-1}$, $k=2\pi/\lambda$ is the wave number in the vacuum and $U_0(x,y,z)=U_{0,0}(x,y)\exp(\mathrm{i}k\delta z)\exp(-k\beta z)$ is the field amplitude along the propagation direction z.

If we define the *complex absorption coefficient* as $\tilde{\mu}\triangleq\tilde{\mu}^R+\mathrm{i}\tilde{\mu}^I\triangleq k(\beta-\mathrm{i}\delta)$ to implicitly include the wave number dependence in $\tilde{\mu}$, then the intensity amplitude becomes

$$\begin{aligned} I_0(x,y,z) &= |U_0(x,y,z)|^2 \\ &= |U_{0,0}(x,y)|^2\exp(-2k\beta z) \\ &= |U_{0,0}(x,y)|^2\exp\left(-2\tilde{\mu}^R z\right), \end{aligned} \tag{1.3}$$

which is the well-known expression of the Beer-Lambert law (Howells et al, 2007).

In both cases, for the electric and intensity fields, Eqs. 1.2 and 1.3 can be rewritten in their derivative expressions as:

$$\begin{aligned} \frac{\mathrm{d}U_0(x,y,z)}{\mathrm{d}z} &= -\tilde{\mu}(x,y,z)U_0(x,y,z) \\ \frac{\mathrm{d}I_0(x,y,z)}{\mathrm{d}z} &= -2\tilde{\mu}^R(x,y,z)I_0(x,y,z). \end{aligned} \tag{1.4}$$

This assumption is only valid for plane waves propagating through a homogeneous medium. However, because scattering effects are negligible, an extended Beer-Lambert law is often used to describe the light attenuation inside specimens with slowly varying absorption coefficients (a quasi-isotropic medium) (Howells et al, 2007).

In this chapter, we will work in the spectral region called *water window*, between the K-absorption edges of carbon (284 eV) and oxygen (543 eV) (Wolter, 1952). In this range, because water (oxygen) is relatively transparent, protein (carbon) and other elements found in biological specimens are much more absorbing. Therefore, proteins are imaged with high contrast and it is possible to visualize hydrated biological specimens near their native state without chemical staining.

1.3 Diffraction theory

To fully understand how the process of wave propagation contributes to image formation, we will make use of the diffraction theory. Although similar developments can be found in many optical textbooks (see Goodman (1996) Chapter 5 as an example), for the sake of clarity we present here the complete development. We begin using the expression of the Fresnel approximation in the Huygens-Fresnel principle, which describes the electric field U^z in the plane z as a function of the electric field U^0 in the reference plane $z=0$ as

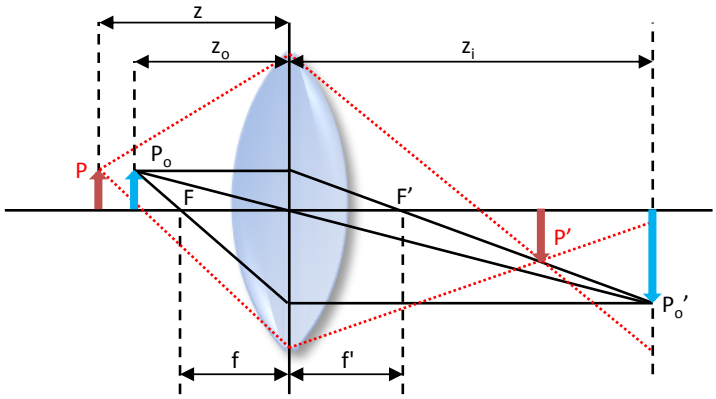

Fig. 1.1 Schematic representation of a standard optical microscope. Plane z_o defines the best-focused plane imaged onto plane z_i, fulfilling $1/z_o + 1/z_i = 1/f$. A source point at P_o is imaged at P'_o. If the source point is shifted to P at plane z, then its image P' is also shifted to a different plane, but in z_i plane P' projects a blob given by the cone limited by the red rays

$$U^z(x,y) = \frac{\exp(\mathrm{i}kz)}{\mathrm{i}\lambda z} \iint U^0(\xi,\eta) \exp\left(\mathrm{i}\frac{k}{2z}\left[(x-\xi)^2 + (y-\eta)^2\right]\right) \mathrm{d}\xi\,\mathrm{d}\eta, \quad (1.5)$$

where (ξ,η) and (x,y) are the point coordinates at planes $z=0$ and z, respectively.

Now, let us suppose the basic scheme of a geometrical optical system (Fig. 1.1), where for an object placed on a plane at a distance z_o from the lens, with a focal length f and complex transmission function $L(x_l,y_l)$, we find a scaled image of the object in a plane at z_i distance from the lens. Theses distances are related by the well-known expression of geometrical optics $1/z_o + 1/z_i = 1/f$. Therefore, for a field distribution $U^o(x,y)$ placed in some plane z, we can obtain the field distribution $U^i(x_i,y_i)$ in the image plane z_i by applying Eq. 1.5 twice: between the z plane and the lens and between the lens and the z_i plane. After eliminating some global phase factors we obtain:

$$U^i(x_i,y_i) = \frac{1}{\lambda^2 z z_i} \iint \left[\iint U^o(x,y) \exp\left(\frac{\mathrm{i}\pi}{\lambda z}\left[(x_l-x)^2 + (y_l-y)^2\right]\right) \mathrm{d}x\mathrm{d}y \right] \times L(x_l,y_l) \exp\left(\frac{\mathrm{i}\pi}{\lambda z_i}\left[(x_i-x_l)^2 + (y_i-y_l)^2\right]\right) \mathrm{d}x_l\mathrm{d}y_l. \quad (1.6)$$

Then, we expand the quadratic phase factors as:

$$U^i(x_i,y_i) = \frac{\exp\left(\frac{\mathrm{i}\pi}{\lambda z_i}\left[x_i^2+y_i^2\right]\right)}{\lambda^2 z z_i} \iint \left[\iint U^o(x,y)\exp\left(\frac{\mathrm{i}\pi}{\lambda z}\left[x^2+y^2\right]\right)\right.$$
$$\left.\times \exp\left(\frac{-\mathrm{i}2\pi}{\lambda z}\left[x x_l + y y_l\right]\right)\mathrm{d}x\mathrm{d}y\right] L(x_l,y_l)\exp\left(\frac{\mathrm{i}\pi}{\lambda}\left[\frac{1}{z}+\frac{1}{z_i}\right]\left[x_l^2+y_l^2\right]\right)$$
$$\times \exp\left(\frac{-\mathrm{i}2\pi}{\lambda z_i}\left[x_i x_l + y_i y_l\right]\right)\mathrm{d}x_l\mathrm{d}y_l. \tag{1.7}$$

If the contribution to an image point (x_i,y_i) were given by a small region of the object around the point $(x_i/M, y_i/M)$, as predicted by geometrical optics (M being the magnification of the optical system defined as $M=-z_i/z$), we could then approximate $\exp\left(\frac{\mathrm{i}\pi}{\lambda z}\left[x^2+y^2\right]\right) \approx \exp\left(\frac{\mathrm{i}\pi}{\lambda z}\left[(x_i/M)^2+(y_i/M)^2\right]\right)$ so that this term could be extracted from the integral (see Goodman (1996) Chapter 5 for a complete explanation). However, we are also interested in planes beyond the DOF where this condition is not fulfilled, and therefore, the previously referenced term cannot be extracted.

For the sake of clarity, let us define $U^{o\prime}(x,y) = U^o(x,y)\exp\left(\frac{\mathrm{i}\pi}{\lambda z}\left[x^2+y^2\right]\right)$; then, Eq. 1.7 becomes

$$U^i(x_i,y_i) \approx \frac{\exp\left(\frac{\mathrm{i}\pi}{\lambda z_i}\left[x_i^2+y_i^2\right]\right)}{\lambda^2 z z_i}$$
$$\times \iint \left[\iint U^{o\prime}(x,y)\exp\left(\frac{-\mathrm{i}2\pi}{\lambda z}\left[x x_l + y y_l\right]\right)\mathrm{d}x\mathrm{d}y\right] L(x_l,y_l)$$
$$\times \exp\left(\frac{\mathrm{i}\pi}{\lambda}\left[\frac{1}{z}+\frac{1}{z_i}\right]\left[x_l^2+y_l^2\right]\right)\exp\left(\frac{-\mathrm{i}2\pi}{\lambda z_i}\left[x_i x_l + y_i y_l\right]\right)\mathrm{d}x_l\mathrm{d}y_l, \tag{1.8}$$

where we have gathered exponential terms. Moreover, because we are interested in the acquired intensity image in plane z_i, the quadratic phase factors outside the integral do not contribute to the final intensity distribution, so they can be dropped.

If we define the *Fourier* transform function $\mathscr{F}$ and its inverse function $\mathscr{F}^{-1}$ as

$$\begin{aligned}\mathscr{F}(f(x)) &\equiv \tilde{f}(u) \triangleq \int f(x)\exp(-2\pi\mathrm{i}xu)\,\mathrm{d}x \\ \mathscr{F}^{-1}\left(\tilde{f}(u)\right) &\equiv f(x) = \int \tilde{f}(u)\exp(2\pi\mathrm{i}xu)\,\mathrm{d}u,\end{aligned} \tag{1.9}$$

then Eq. 1.8 leads to

$$U^i(x_i,y_i) = \frac{1}{\lambda^2 z z_i}\iint \tilde{U}^{o\prime}\left(\tfrac{x_l}{\lambda z},\tfrac{y_l}{\lambda z}\right) L(x_l,y_l)\exp\left(\frac{\mathrm{i}\pi}{\lambda}\left[\frac{1}{z}+\frac{1}{z_i}\right]\left[x_l^2+y_l^2\right]\right) \times\exp\left(\frac{-\mathrm{i}2\pi}{\lambda z_i}\left[x_i x_l + y_i y_l\right]\right)\mathrm{d}x_l\mathrm{d}y_l, \tag{1.10}$$

where $\tilde{U}^{o\prime}(f_x,f_y)$ is the *Fourier* transform of the field distribution $U^{o\prime}(x,y)$ evaluated at $(f_x=\frac{x_l}{\lambda z}, f_y=\frac{y_l}{\lambda z})$.

If we analyze Eq. 1.10 in *Fourier* space, we see that

$$\tilde{U}^i(f_{x_i},f_{y_i}) = \frac{1}{\lambda^2 z z_i}\tilde{U}^{o\prime}\left(Mf_{x_i},Mf_{y_i}\right)(\lambda z_i)^2 \times L(-\lambda z_i f_{x_i},-\lambda z_i f_{y_i})\exp\left(\frac{\mathrm{i}\pi}{\lambda}\left[\frac{1}{z}+\frac{1}{z_i}\right]\left[(\lambda z_i f_{x_i})^2+(\lambda z_i f_{y_i})^2\right]\right), \tag{1.11}$$

that is, the *Fourier* transform of the field distribution at the sensor plane z_i is a scaled version of the *Fourier* transform of the field distribution at plane z in object space multiplied by the lens function and a quadratic phase factor, evaluated at frequencies $\left(f_{x_i}=\frac{-x_l}{\lambda z_i}, f_{y_i}=\frac{-y_l}{\lambda z_i}\right)$. Eq. 1.11 can also be expressed as a convolution in real space. To do so, we have to reduce the object-image relation to a convolution equation by normalizing the object coordinates of the *Fourier* transforms to remove inversion and magnification:

$$U^i(x_i,y_i) = \frac{1}{\lambda^2 z z_i}\iint \frac{1}{|M|^2}U^{o\prime}\left(\tfrac{\xi}{M},\tfrac{\eta}{M}\right)(\lambda z_i)^2\mathscr{F}^{-1}_{f_{x_i},f_{y_i}}\Big\{L(-\lambda z_i f_{x_i},-\lambda z_i f_{y_i}) \exp\left(\frac{\mathrm{i}\pi}{\lambda}\left[\frac{1}{z}+\frac{1}{z_i}\right]\left[(\lambda z_i f_{x_i})^2+(\lambda z_i f_{y_i})^2\right]\right)\exp\left(-\mathrm{i}2\pi(f_{x_i}\xi+f_{y_i}\eta)\right)\Big\}\mathrm{d}\xi\mathrm{d}\eta, \tag{1.12}$$

where $\mathscr{F}^{-1}_{f_{x_i},f_{y_i}}$ denotes the inverse *Fourier* transform operation in plane (f_{x_i},f_{y_i}).

Because $L(x,y)$ is zero outside the lens aperture, the $\mathscr{F}^{-1}_{f_{x_i},f_{y_i}}\{\cdot\}$ argument in Eq. 1.12 is an integrable continuous function. Then, applying the *Fourier* inversion theorem $\mathscr{F}_{x,y}\{f(x,y)\}=\mathscr{F}^{-1}_{x,y}\{f(-x,-y)\}$ (Folland, 1992), $U^i(x_i,y_i)$ can be expressed as the convolution

$$U^i(x_i,y_i) = \frac{1}{|M|}U^{o\prime}\left(\tfrac{x_i}{M},\tfrac{y_i}{M}\right)\underset{x_i,y_i}{\otimes} \mathscr{F}_{f_{x_i},f_{y_i}}\left\{L(\lambda z_i f_{x_i},\lambda z_i f_{y_i})\exp\left(\frac{\mathrm{i}\pi}{\lambda}\left[\frac{1}{z}+\frac{1}{z_i}\right]\left[(\lambda z_i f_{x_i})^2+(\lambda z_i f_{x_i})^2\right]\right)\right\}, \tag{1.13}$$

where $\underset{x_i,y_i}{\otimes}$ is the symbol to denote the convolution operation in the (x_i,y_i) plane.

Let us rewrite the field distribution in plane z_i as the following object-image relationship:

$$U^i(x,y) = U_g(x,y) \underset{x,y}{\otimes} \tilde{h}(x,y,z), \tag{1.14}$$

where $U_g(x,y)$ is the ideal image predicted by geometrical optics, and $\tilde{h}(x,y,z)$ is the impulse response, also called the point spread function (*PSF*), of the lens related to an imaged object placed in plane z and imaged in plane z_i. Then, comparing Eq. 1.13 and Eq. 1.14, we set the following definitions:

$$\begin{aligned} U_g(x,y) &= \frac{1}{|M|} U^{o\prime}\left(\tfrac{x}{M}, \tfrac{y}{M}\right), \\ \tilde{h}(x,y,z) &= \mathscr{F}_{f_x,f_y}\left\{ L(\lambda z_i f_x, \lambda z_i f_y) \exp\left(\frac{\mathrm{i}\pi}{\lambda}\left[\frac{1}{z} + \frac{1}{z_i}\right]\left[(\lambda z_i f_x)^2 + (\lambda z_i f_y)^2\right]\right)\right\}, \end{aligned} \tag{1.15}$$

and the intensity measured in the sensor plane is

$$I^i(x,y) = \left| U_g(x,y) \underset{x,y}{\otimes} \tilde{h}(x,y,z) \right|^2. \tag{1.16}$$

In the case of totally incoherent illumination, the intensity given by Eq. 1.16 is well-known to become (Goodman, 1996)

$$I^i(x,y) = I_g(x,y) \underset{x,y}{\otimes} \left|\tilde{h}(x,y,z)\right|^2. \tag{1.17}$$

where $I_g(x,y) = \left|U_g(x,y)\right|^2 = \frac{1}{|M|^2}\left|U^o(\frac{x}{M}, \frac{y}{M})\right|^2$ is the ideal intensity distribution given by geometrical optics and is directly related to the intensity distribution at the object plane where the quadratic phase factor in the definition of $U^{o\prime}$ has been canceled.

In summary, the intensity distribution in the image plane is the one we would measure if we had an infinite ideal lens convolved with the Fraunhofer diffraction pattern of the lens aperture combined with a quadratic phase factor that takes into account the effect of the object being in a plane different from the focused plane z_o.

1.4 Image forming systems

In a first-order approximation, there is an agreement to model full-field transmission X-ray microscopes as systems formed by a single ideal lens illuminated by a parallel wave (Weiss et al, 2000). Therefore, within this approximation, the only source of aberration is the limited size of the lens, i.e., the aperture of the objective lens. Because the microscope imaging system collects only a fraction of the light emitted by a given point, it cannot focus the light into a perfect three-dimensional image of the point. Instead, the point appears widened and spread out by the previously introduced three-dimensional *PSF*.

1.4.1 Ideal lens

The complex transmission function of a finite lens of focal distance f is defined as

$$L(x,y) = T(x,y)\exp\left(-\frac{\mathrm{i}k}{2f}\left[x^2+y^2\right]\right), \tag{1.18}$$

where $T(x,y)$ is the function that defines the aperture of the lens, which, in most cases, is usually a circular aperture of radius R, defined by the circ function

$$\mathrm{circ}\left(\frac{x}{R},\frac{y}{R}\right) = \begin{cases} 1 & \sqrt{x^2+y^2} \le R \\ 0 & \sqrt{x^2+y^2} > R. \end{cases} \tag{1.19}$$

If we substitute Eq. 1.18 into Eq. 1.15, we obtain

$$\tilde{h}(x,y,z) = \mathscr{F}_{f_x,f_y}\left\{ \mathrm{circ}\left(\frac{\lambda z_i f_x}{R},\frac{\lambda z_i f_y}{R}\right)\exp\left(\frac{\mathrm{i}\pi}{\lambda}D(z)\left[(\lambda z_i f_x)^2+(\lambda z_i f_y)^2\right]\right)\right\}, \tag{1.20}$$

where we have defined the *Defocus* of the optical system as

$$D(z) = \frac{1}{z}+\frac{1}{z_i}-\frac{1}{f} = \frac{1}{z}-\frac{1}{z_o}. \tag{1.21}$$

Substituting Eq. 1.20 into Eq. 1.17 and defining the point spread function for the totally incoherent case as

$$h \triangleq \left|\tilde{h}\right|^2, \tag{1.22}$$

we easily see that the *PSF* of an ideal lens for the incoherent case is

$$h(x,y,z) = \left| \pi\left(\frac{R}{\lambda z_i}\right)^2 \frac{J_1\left(\frac{2\pi R}{\lambda z_i}r\right)}{\frac{\pi R}{\lambda z_i}r} \underset{x,y}{\otimes} \frac{\mathrm{i}}{D(z)\lambda z_i^2}\exp\left(-\frac{\mathrm{i}\pi\lambda}{D(z)}\left[\left(\frac{x}{\lambda z_i}\right)^2+\left(\frac{y}{\lambda z_i}\right)^2\right]\right)\right|^2, \tag{1.23}$$

where $r=\sqrt{x^2+y^2}$ and J_1 is a Bessel function of the first kind. This Eq. 1.23 is a well-known expression (see Mielenz (1999) and Weiss et al (2000)), and in the case of no defocus ($D(z)=0$) it is known as the *Airy disk* pattern. As an example, the 3D *PSF* of the ideal lens used in Section 1.7 is shown in Fig. 1.2.

If we define the *amplitude transfer function H* of an optical system as

$$H(f_x,f_y,z) = \mathscr{F}_{x,y}\left\{\tilde{h}(x,y,z)\right\}, \tag{1.24}$$

then, analyzing the expression of Eq. 1.20 in *Fourier* space, we arrive at

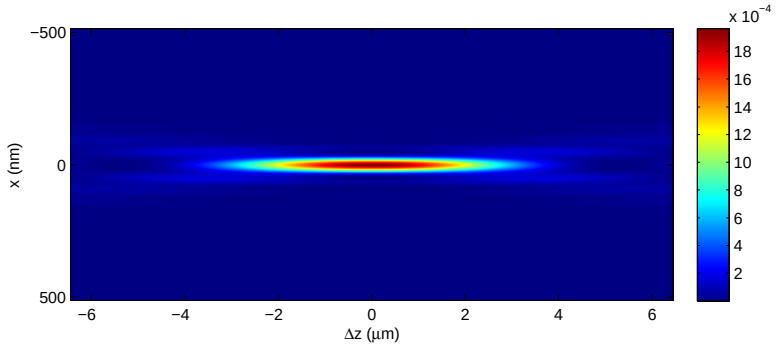

Fig. 1.2 3D intensity point spread function of an ideal lens of 1.47 mm focal length, 44.8 μm radius and 48.8 nm maximum resolution (lens equivalent to a Fresnel zone plate of 560 zones and a 40 nm outer zone width), with an illumination wavelength of 2.43 nm. Each column represents the values of a *PSF* profile according to the defocus $D(z)$, where $\Delta z = z - z_o$. The dependence in y is the same as in x

$$H(f_x, f_y, z) = \text{circ}\left(\frac{\lambda z_i f_x}{R}, \frac{\lambda z_i f_y}{R}\right) \exp\left(\frac{i\pi}{\lambda} D(z)\left[(\lambda z_i f_x)^2 + (\lambda z_i f_y)^2\right]\right). \quad (1.25)$$

Furthermore, the equivalent in a totally incoherent illumination system is $\mathscr{H}$, known as the *optical transfer function*, and is related to $H(f_x, f_y, z)$ by Eq. 1.22, resulting in:

$$\mathscr{H}(f_x, f_y, z) = \mathscr{F}_{x,y}\{h(x, y, z)\} = H(f_x, f_y, z) \underset{x,y}{\star} H(f_x, f_y, z), \quad (1.26)$$

where $\underset{x,y}{\star}$ denotes the autocorrelation symbol in the plane (x, y). Fig. 1.3 shows the amplitude of $\mathscr{H}$ for the *PSF* introduced in Fig. 1.2 for several values of defocus Δz from the plane z_o.

1.4.2 Fresnel zone plate lens

Thus far, we have assumed that the *PSF* of an X-ray microscope is properly approximated by the *PSF* of a perfect system computed at the focal point. In this subsection, we discuss how similar the *PSF* of a perfect system is to the one provided by a Fresnel zone plate (FZP), which is the imaging lens actually used in an X-ray microscope.

A Fresnel zone plate is a diffractive optical element formed by concentric rings whose width decreases as the radius increases in such a way that light focuses at points where there is a constructive interference. In fact, an FZP is considered a transmission grating in terms of the radius squared. Therefore, the function that defines this grating can be represented by a *Fourier* series expansion (Attwood, 2007). Then, the transmission complex function of a Fresnel zone plate in the aperture of

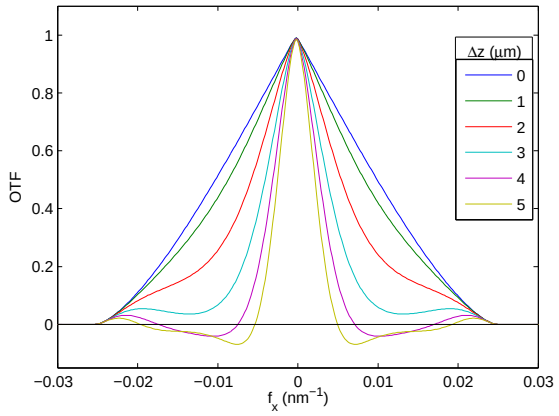

Fig. 1.3 Profiles of the optical transfer function corresponding to the ideal lens *PSF* of Fig. 1.2 for several values of Δz (Defocus)

the optical system can be written as an infinite series of ideal lenses multiplied by the aperture function:

$$L_{FZP}(x,y) = \operatorname{circ}\left(\frac{x}{R},\frac{y}{R}\right)\sum_{m=-\infty}^{\infty}\sqrt{\eta_m}\exp\left(-\frac{\mathrm{i}\pi}{\lambda f_m}\left[x^2+y^2\right]\right), \tag{1.27}$$

where $f_m = f/m$ are the focal lengths for each diffracted order m, and the coefficients η_m are the diffractive efficiencies given by

$$\eta_m = \begin{cases} 1/4 & m=0 \\ 1/m^2\pi^2 & m \text{ odd} \\ 0 & m \text{ even} \end{cases}. \tag{1.28}$$

Therefore, if we set the microscope to focus the image given by the first order of diffraction of the Fresnel zone plate, we will also be acquiring the unfocused images for the rest of the orders. Thus far, we have assumed that these contributions are negligible. To validate this assumption, we use the numerical method given by Mendoza-Yero et al (2010):

$$\begin{aligned}\tilde{h}_{FZP}(\mathbf{r},z) &\propto \int_0^{\infty} T(\rho)\exp\left(\frac{\mathrm{i}\pi}{\lambda}\left[\frac{1}{z}+\frac{1}{z_i}\right]\rho^2\right)J_0\left(\frac{k}{z_i}\rho\mathbf{r}\right)\rho\,\mathrm{d}\rho \\ &\approx \frac{1}{2\pi(z+z_i)}\sum_{n=1}^{N/2}\exp\left(\frac{\mathrm{i}\pi}{\lambda}\left[\frac{1}{z}+\frac{1}{z_i}\right]\rho^2\right)J_0\left(\frac{k}{z_i}\rho\mathbf{r}\right)\Bigg|_{\rho=r_n^{in}}^{\rho=r_n^{out}}\end{aligned} \tag{1.29}$$

where $\tilde{h}_{FZP}(\mathbf{r},z)$ is the point spread function in cylindrical coordinates, J_0 denotes the Bessel function of zero order and r_n^{in} and r_n^{out} are the inner and outer radius of

the n zone of the Fresnel plate. In that work, several point spread functions were computed using an illumination wavelength of $\lambda = 2.43$ nm and a zone plate with 560 zones, a radius of 44.8 µm and an outer zone width of 40 nm (these parameters correspond to a typical setup of the X-ray microscopes at the Bessy II and ALBA synchrotrons). Fig. 1.4(a) compares the *PSF* functions obtained by Mendoza-Yero et al (2010) with the corresponding profiles extracted from Fig. 1.2. For the sake of comparison, the *PSF* profiles for the Fresnel zone plate have been intensity normalized to the *in-focus* profile, as the height of the Fresnel zone plate profiles would

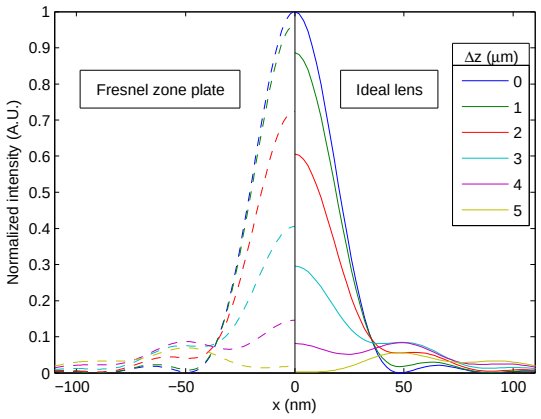

(a)

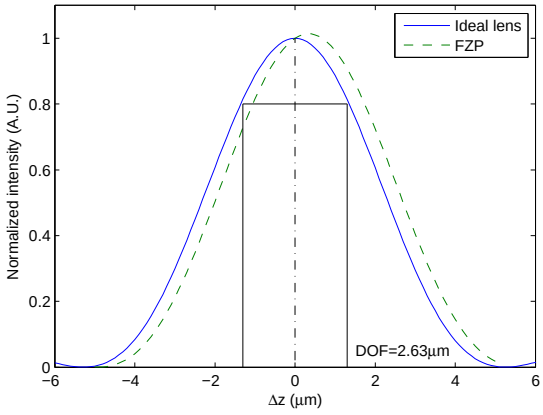

(b)

Fig. 1.4 Comparison of the *PSF* for the ideal lens used in Fig. 1.2 and a numerical simulation of the corresponding Fresnel zone plate with an outer zone width of 40 nm and 560 zones. (a) Profiles in planes (x,y) for different defocus (Δz) values; (b) Profiles along the optical axis z centered on the "best focusing plane" z_o

be much lower because the efficiency for the first-order lens is only approximately 10% (see Eq. 1.28). As shown, the general aspect and behavior (for example, maxima and minima localization) are very similar, although the actual values differ. These differences are understood when analyzing Fig. 1.4(b).

In Fig. 1.4(b), we further analyze the intensity distributions measured in the sensor for test points placed along the optical axis. We see that both profiles have the same shape, but the profile of the Fresnel zone plate is shifted approximately 300 nm, suggesting an apodizing effect responsible for the mismatching of the peak intensity values at both sides in Fig. 1.4(a) for different Δz values.

1.4.2.1 *Off-axis* image formation

PSFs of real optical systems depend on the distance from the observed point of the sample to the optical axis. The diffraction pattern that arises from an *off-axis* point is not symmetrically truncated by the aperture of the lens, introducing a certain amount of coma aberration. In this chapter, the diffractive optics calculations between the sample plane and the lens we present are based on the Fresnel approximation, i.e., X-rays propagate with a small divergence angle. Under these conditions, we have assumed that the *PSF* is independent of the position of the sample point to be convolved with. The validity of these assumptions has been proven in the work of Sypek et al (2010). In that work, using numerical computation, several *PSFs* were simulated for several points at different (i) distances from the optical axis and (ii) defocuses (Figure 1.5). The simulated conditions are identical to those described in Section 1.4.2. The results prove that the *PSF* does not change significantly

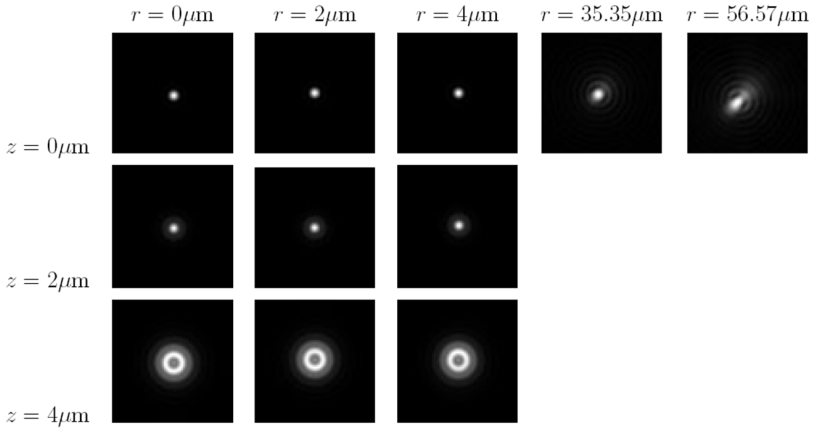

Fig. 1.5 *PSF* distributions for different distances *r* from the optical axis and defocusing *z* simulated for a Fresnel zone plate of 560 zones and a 40 nm outer zone width (Reproduced with permission from Sypek et al (2010))

for points closer than 15 μm to the optical axis, and significant aberrations appear only for points located far from the optical axis. Therefore, to assume a constant 3D *PSF* seems to be reasonable in soft X-ray tomography.

Therefore, to assume that the *PSF* of an ideal lens is, indeed, the experimental *PSF* is a good first-order approximation. However, further quantitative works in TomoX may require working with *PSF* calculations in a numerical manner.

1.5 Depth of field

The term *depth of field* refers to the region around plane z_o in the object space that renders an acceptably sharp image into the sensor plane z_i, whereas *depth of focus* applies to the conjugated region around plane z_i in the image space where an object placed in plane z_o is acceptably imaged. Although in the literature *depth of focus* is widely used indistinctly of *depth of field*, in this chapter we favor the use of the latter term (Jacobson et al, 2001).

In the previous section, we showed the plot of the measured intensities for points around the best focus plane obtained from numerical calculations. In this section, we report an analytical description of the intensity in the field region based on the development carried out by Martínez-Corral and Zapata-Rodríguez (1998).

Let us start by propagating an ideal point source placed in the optical axis $U^o(x,y) = \delta(0,0)$ for z values around z_o using Eq. 1.10 evaluated at $(x_i = 0, y_i = 0)$, where the lens function $L(x_l, x_l)$ has been substituted by the expression of the ideal lens described in Eq. 1.18:

$$U^i_{0,0}(z) \equiv U^i(0,0,z) = \frac{\exp\left(\mathrm{i}k\left(z+z_i\right)\right)}{\lambda^2 z z_i} \iint T(x_l,y_l) \exp\left(\frac{\mathrm{i}\pi}{\lambda}\left(x_l^2+y_l^2\right)D\right) \mathrm{d}x_l \mathrm{d}y_l, \tag{1.30}$$

where the aperture T is the circ function.

Then, changing to polar coordinates, we have:

$$T(x_l,y_l) \to \mathscr{T}(\mathbf{r}_l,\theta) = \mathscr{T}(\mathbf{r}_l) = \operatorname{circ}\left(\frac{\mathbf{r}_l}{R}\right) = \begin{cases} 1 & r_l \le R \\ 0 & r_l > R \end{cases}$$

$$U^i_{0,0}(z) = \frac{\exp\left(\mathrm{i}k\left(z+z_i\right)\right)}{\lambda^2 z z_i} \int_0^\infty \int_0^{2\pi} \mathscr{T}(\mathbf{r}_l) \exp\left(\frac{\mathrm{i}\pi}{\lambda} r^2 D\right) r_l \mathrm{d}r_l \mathrm{d}\theta, \tag{1.31}$$

followed by a variable change:

$$\zeta = r^2; \qquad \mathrm{d}\zeta = 2r\mathrm{d}r$$
$$\mathscr{T}(r) \to t(\zeta) = \begin{cases} 1 & \zeta \leq R^2 \\ 0 & \zeta > R^2. \end{cases} \tag{1.32}$$

In this way, we arrive at the following expression for the field amplitude:

$$\begin{aligned} U^i_{0,0}(z) &= \frac{\exp(\mathrm{i}k(z+z_i))}{\lambda^2 z z_i}\pi \int_0^\infty t(\zeta)\exp\left(\mathrm{i}2\pi\frac{D}{2\lambda}\zeta\right)\mathrm{d}\zeta \\ &= \frac{\exp(\mathrm{i}k(z+z_i))}{\lambda^2 z z_i}\pi \exp\left(\mathrm{i}\pi R^2\frac{D}{2\lambda}\right) R^2\ \mathrm{sinc}\left(R^2\frac{D}{2\lambda}\right). \end{aligned} \tag{1.33}$$

where $\mathrm{sinc}(x) = sin(\pi x)/\pi x$.

Eq. 1.33 shows that the field amplitude for the point source along the z axis is proportional to the *Fourier* transform of the aperture evaluated at frequency ($u = R^2 D/2\lambda$). Hence, the intensity distribution normalized at plane $z = z_o$ is

$$I^{i,N}_{0,0}(z) = \left(\frac{z_o}{z}\right)^2 \mathrm{sinc}\left(\frac{R^2}{2\lambda}D\right)^2. \tag{1.34}$$

Let us use the definition of depth of field given by Born and Wolf (1999), which is described as the distance where 20% of the maximum axial intensity is lost. Because the $\mathrm{sinc}(R^2 D/2\lambda)^2$ term decreases much faster than $(z_o/z)^2$, we can approximate the intensity distribution to

$$I^{i,N}_{0,0}(z) \approx \mathrm{sinc}\left(\frac{R^2}{2\lambda}D\right)^2, \tag{1.35}$$

and let us define $\alpha_{0.8}$ as the sinc argument, which fulfills $\mathrm{sinc}(\pm\alpha_{0.8})^2 = 0.8$. Therefore, the values of z for this condition are given by

$$\begin{aligned} &\frac{R^2}{2\lambda}D = \frac{R^2}{2\lambda}\left[\frac{1}{z} - \frac{1}{z_o}\right] = \pm\alpha_{0.8} \\ &z_{\pm\alpha_{0.8}} = \frac{z_o R^2}{R^2 \pm 2\lambda z_0 \alpha_{0.8}}. \end{aligned} \tag{1.36}$$

Taking into account the definition of depth of field, we arrive at

$$\Delta z_{dof} = z_{-\alpha_{0.8}} - z_{+\alpha_{0.8}} = \frac{4 z_o^2 R^2 \lambda\, \alpha_{0.8}}{R^4 - (2 z_o \lambda\, \alpha_{0.8})^2}. \tag{1.37}$$

In a typical experimental setting, such as the ideal lens used in Fig. 1.2, $\lambda \approx 10^{-9}$ m, $f = 1.43$ mm, $R \approx 50\,\mu$m, and $z_0 \approx 1.5$ mm. Due to $\alpha_{0.8} \approx 0.25$, the denominator can be approximated to R^4, and

$$\Delta z_{dof} \approx \frac{z_o^2 \lambda}{R^2}. \tag{1.38}$$

Substituting the values of our test ideal lens from Fig. 1.2, we obtain $\Delta z_{dof} = 2.63\ \mu\text{m}$.

Eq. 1.34 analytically describes the shape of the axial distribution numerically calculated for an ideal lens (plotted in Fig. 1.4(b)). Eq. 1.38 shows that the theoretical depth of field for an ideal lens depends only on the distance from the lens to the best focusing plane, the illumination wavelength and the radius of the lens. These results agree with the studies that aimed to obtain an analytical expression based on the Debye integral through the Lommel functions (see Born and Wolf (1999) Section 8.8.1). However, the formulation we introduce here also includes the factor $(z_o/z)^2$, which introduces a shift on the plane z, whose intensity measured in the sensor plane is maximum in the case of low numerical aperture lenses, while the equivalent formula in terms of Lommel functions is not.

1.6 Image formation in an X-ray microscope

The general field of X-ray microscopy is large, with quite different instruments tuned to particular applications. We find different lens-based microscopes, such as those used in full-field transmission X-ray microscopy (TXM), scanning transmission X-ray microscopy (STXM), scanning photoelectron microscopy, micro-X-ray fluorescence (μ-XRF) spectroscopy, and synchrotron radiation X-ray tomographic microscopy (SRXTM). These devices are based on the use of Fresnel zone plates, multilayer Laue lens, multilayer coated Schwarschild reflective optics or elliptically bent mirrors as imaging systems (Sakdinawat and Attwood, 2010). Moreover, there are schemes where no lenses are used to form images, with the information recovered by holographic and phase retrieval methods (Chapman and Nugent, 2010; Nelson et al, 2010). These microscopes use synchrotron radiation as source of illumination, but today we can also find an increasing number of X-ray microscopes in laboratories that are based on plasma sources (Legall et al, 2012; Bertilson et al, 2011). In our case, the image model proposed is based on the scheme of the *TXM*. Furthermore, this model considers the sample illuminated by a plane wavefront without taking into account the characteristics of the collimator lens. This is essentially true because the sample is usually placed in the plane where the image of the source is focused. Moreover, we consider that the illumination that arrives at the specimen is totally incoherent, independently of the numerical apertures matching. Today, there are operative X-ray microscopes for cellular biology at Alba (Barcelona), Bessy II (Berlin) and ALS (Berkeley). Their specifications and design vary, with the MISTRAL microscope at ALBA and XM-2 at ALS probably conforming more closely to our modeling considerations.

The image formation process we are introducing assumes that the specimen dimensions are on the order of the DOF of the optical system, leading to an expression

that relates the measured projection to the absorption coefficients of the sample and the *PSF* of the microscope. Furthermore, we analyze the approximations when the specimen is much smaller —in which case the *PSF* is assumed constant— and when the *PSF* can be neglected, arriving at well-known expressions.

1.6.1 Image formation model with z-dependent point spread function

To understand how the intensity image acquired by the camera in the sensor plane z_i is formed, we need to find an expression that connects it to the complex absorption coefficients $\tilde{\mu}$, which define the 3D information of the sample. We begin from Eq. 1.14, which relates the electromagnetic field at planes $z = z_i$ and $z = z'$ in the absence of any specimen, with z' a plane in the object space before the lens. Note that it is not assumed that planes z' and z_i fulfill the lens equation $1/z_o - 1/z_i = 1/f$, that is, that plane z' may be out of focus, so the equation remains valid even in that case.

In Fig. 1.6, we show the schema of the microscope. Let us assume that the sample is truncated by the plane at z'. By conceptually removing the piece of sample between plane z' and the lens, we can measure the field distribution $U^{z_i}(x,y,z')$ in plane z_i related to the field distribution in plane z' by Eq. 1.14 as

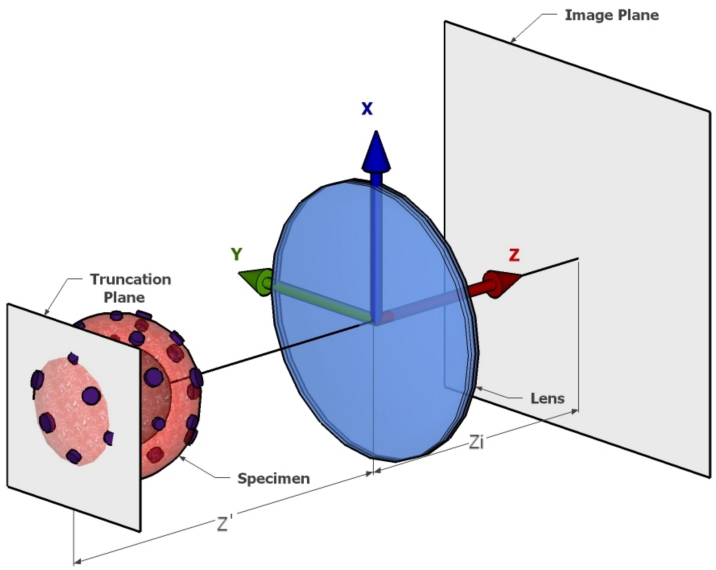

Fig. 1.6 Schematic representation of an X-ray microscope where a specimen is placed in object space. The plane at z' defines the integration variable and allows calculation of how the specimen contributes to the projection (Reproduced with permission from Oton et al (2012))

$$U^{z_i}(x,y,z') = U_g^{z_i}(x,y,z') \underset{x,y}{\otimes} \tilde{h}(x,y,z'). \tag{1.39}$$

For a specimen that fulfills the conditions described in Section 1.2, the field in the outgoing plane for any slice of the specimen is defined as a function of the field in the incoming plane by Eq. 1.4 as

$$U^o(x,y,z'+\Delta z') \approx (1-\tilde{\mu}(x,y,z')\Delta z')U^o(x,y,z'). \tag{1.40}$$

The electric field distribution U^o in the backplane $z'+\Delta z'$ of a slice z' leads to calculating the field distribution in the sensor plane U^{z_i} for this $z'+\Delta z'$ value by substituting Eq. 1.40 into Eq. 1.39 through the definition of $U_g^{z_i}$ in Eq. 1.15:

$$\begin{aligned} U^{z_i}(x,y,z'+\Delta z') &= U_g^{z_i}(x,y,z'+\Delta z') \underset{x,y}{\otimes} \tilde{h}(x,y,z'+\Delta z')) \\ &= \left[(1-\tilde{\mu}_g(x,y,z')\Delta z')U_g^{z_i}(x,y,z')\right] \underset{x,y}{\otimes} \tilde{h}(x,y,z'+\Delta z'), \end{aligned} \tag{1.41}$$

where $\tilde{\mu}_g(x,y,z') = \tilde{\mu}(\frac{x}{M},\frac{y}{M},z')$.

By definition, the intensity measured by the photodetector is

$$I^{z_i}(x,y,z'+\Delta z') = \left\langle U^{z_i}(x,y,z'+\Delta z')U^{z_i*}(x,y,z'+\Delta z')\right\rangle \tag{1.42}$$

where $\langle f(t)\rangle = \frac{1}{T}\int_0^T f(t)\mathrm{d}t$ is the time-average operator. Although not explicitly shown here, all waves have a time dependence given by a factor $\exp(-\mathrm{i}2\pi ft)$, where f is the frequency of the wave.

If we combine Eqs. 1.41 and 1.42, taking into account the totally incoherent illumination case, we obtain that

$$\begin{aligned} I^{z_i}(x,y,z'+\Delta z') &= \left[\left|1-\tilde{\mu}_g(x,y,z')\Delta z'\right|^2 I_g^{z_i}(x,y,z')\right] \underset{x,y}{\otimes} \left|\tilde{h}(x,y,z'+\Delta z')\right|^2 \\ &= \Big[\left(1-\left[\tilde{\mu}_g^R(x,y,z') - \mathrm{i}\tilde{\mu}_g^I(x,y,z')\right]\Delta z'\right) \\ &\quad \left(1-\left[\tilde{\mu}_g^R(x,y,z') + \mathrm{i}\tilde{\mu}_g^I(x,y,z')\right]\Delta z'\right) I_g^{z_i}(x,y,z')\Big] \\ &\quad \underset{x,y}{\otimes} \left|\tilde{h}(x,y,z'+\Delta z')\right|^2 \\ &= \left[\left(1-2\tilde{\mu}_g^R(x,y,z')\Delta z' + O\left(\Delta z'^2\right)\right) I_g^{z_i}(x,y,z')\right] \\ &\quad \underset{x,y}{\otimes} \left|\tilde{h}(x,y,z'+\Delta z')\right|^2 \end{aligned} \tag{1.43}$$

where $O(x^2)$ refers to second-order terms (the derivation of Eq. 1.43 is detailed in the Appendix). In the case of the water window, $O(\Delta z'^2)$ can be neglected, being the only component of $\tilde{\mu}$ that remains its real part. This means that soft X-ray microscope projections under totally incoherent illumination are only produced by absorption, and therefore, any phase shift is negligible.

Defining the *intensity absorption coefficient* as $\mu \triangleq 2\tilde{\mu}_g^R$, Eq. 1.43 leads to

$$
\begin{aligned}
I^{z_i}(x,y,z'+\Delta z') &\approx \left[(1-\mu(x,y,z')\Delta z')\right] I_g^{z_i}(x,y,z') \underset{x,y}{\otimes} \left|\tilde{h}(x,y,z'+\Delta z')\right|^2 \\
&= I_g^{z_i}(x,y,z') \underset{x,y}{\otimes} \left|\tilde{h}(x,y,z'+\Delta z')\right|^2 \\
&\quad -\mu(x,y,z') I_g^{z_i}(x,y,z') \underset{x,y}{\otimes} \left|\tilde{h}(x,y,z'+\Delta z')\right|^2 \Delta z'. \qquad (1.44)
\end{aligned}
$$

Let us apply the definition of the intensity *PSF* h given in Eq. 1.22. If we assume h is a slowly varying function along z, then $h(x,y,z'+\Delta z') \approx h(x,y,z')$, and identifying the expression of $I^{z_i}(x,y,z')$ described by Eq. 1.16, we arrive at

$$
I^{z_i}(x,y,z'+\Delta z') = I^{z_i}(x,y,z') - \mu(x,y,z') I_g^{z_i}(x,y,z') \underset{x,y}{\otimes} h(x,y,z'+\Delta z')\Delta z', \qquad (1.45)
$$

therefore, after rearranging some factors,

$$
\frac{I^{z_i}(x,y,z'+\Delta z') - I^{z_i}(x,y,z')}{\Delta z'} = -\mu(x,y,z') I_g^{z_i}(x,y,z') \underset{x,y}{\otimes} h(x,y,z'+\Delta z') \qquad (1.46)
$$

and taking the limit when $\Delta z' \to 0$

$$
\frac{\mathrm{d}I^{z_i}(x,y,z')}{\mathrm{d}z'} = -\mu(x,y,z') I_g^{z_i}(x,y,z') \underset{x,y}{\otimes} h(x,y,z'). \qquad (1.47)
$$

This equation can be rewritten in integral form:

$$
\begin{aligned}
I^{z_i}(x,y,z_A) &= I^{z_i}(x,y,z_B) - \int_{z_B}^{z_A} \left[\mu(x,y,z') I_g^{z_i}(x,y,z')\right] \underset{x,y}{\otimes} h(x,y,z')\mathrm{d}z' \\
&= I^{z_i}(x,y,z_B) \\
&\quad - \int_{z_B}^{z_A} \left[\mu(x,y,z') I_g^{z_i}(x,y,z_B) \mathrm{e}^{-\int_{z_B}^{z'} \mu(x,y,\xi)\mathrm{d}\xi}\right] \underset{x,y}{\otimes} h(x,y,z')\mathrm{d}z' \qquad (1.48)
\end{aligned}
$$

where z_B is a point before the specimen and z_A is a point after the specimen but before the lens.

In the following, we will simplify Eq. 1.48 for those cases in which either the specimen is fully in focus (electron microscopy) or the *PSF* can be ignored (Computerized Axial Tomography in Biomedicine).

1.6.2 The EM tomography case: Image formation model with z-constant point spread function

For the case where the specimen is fully in focus, which is a common assumption in the related field of Electron Tomography, the *PSF* is considered independent of plane z. Therefore, in Eq. 1.48 h can be extracted from the integral and then solved analytically using the *Second Fundamental Theorem of Calculus* ($F(x) = \int_a^x f(s)\mathrm{d}s$ then $\mathrm{d}F(x)/\mathrm{d}x = f(x)$), writing Eq. 1.48 as

$$\begin{aligned} I^{z_i}(x,y,z_A) &= \left[I_g^{z_i}(x,y,z_B) \left(1 - \int_{z_B}^{z_A} \mu(x,y,z) \mathrm{e}^{-\int_{z_B}^{z} \mu(x,y,\xi)\mathrm{d}\xi} \mathrm{d}z \right) \right] \underset{x,y}{\otimes} h(x,y) \\ &= \left[I_g^{z_i}(x,y,z_B) \mathrm{e}^{-\int_{z_B}^{z_A} \mu(x,y,\xi)\mathrm{d}\xi} \right] \underset{x,y}{\otimes} h(x,y) \end{aligned} \tag{1.49}$$

Recalling that μ is the 3D distribution of the intensity absorption coefficients we are interested in recovering, and operating in the previous formula, we arrive at:

$$\int_{z_B}^{z_A} \mu(x,y,\xi)\mathrm{d}\xi = -\ln \left(\frac{I^{z_i}(x,y,z_A) \underset{x,y}{\otimes} h^{-1}(x,y))}{I^{z_i}(x,y,z_B) \underset{x,y}{\otimes} h^{-1}(x,y)} \right) \tag{1.50}$$

where $h^{-1}(x,y)$ is a function such that $h(x,y) \underset{x,y}{\otimes} h^{-1}(x,y) = \delta(x,y)$. Eq. 1.50 indicates that in *Fourier* space the intensity distributions measured with and without a specimen, $I^{z_i}(x,y,z_A)$ and $I^{z_i}(x,y,z_B)$, respectively, are being corrected with the inverse of the optical transfer function $H^{-1}(f_x,f_y) = \mathscr{F}_{x,y}\left\{h^{-1}(x,y)\right\}$. Naturally, in practical terms the direct inversion by h^{-1} may be difficult to implement directly, and several methods, such *Wiener* filtration (Frank, 2006), may be used instead.

1.6.3 The CT case: Image formation model with δ-like point spread function

In those cases in which the *PSF* can be ignored —for instance, in Computerized Axial Tomography in Biomedicine— then h can be substituted by a Dirac's δ in Eq. 1.49, leading to

$$\begin{aligned} I^{z_i}(x,y,z_A) &= \left[I_g^{z_i}(x,y,z_B) \mathrm{e}^{-\int_{z_B}^{z_A} \mu(x,y,\xi)\mathrm{d}\xi} \right] \underset{x,y}{\otimes} \delta(x,y) \\ &= I_g^{z_i}(x,y,z_B) \mathrm{e}^{-\int_{z_B}^{z_A} \mu(x,y,\xi)\mathrm{d}\xi}. \end{aligned} \tag{1.51}$$

Therefore, the absorption coefficients of the specimen are directly related to the intensity images by

$$\int_{z_B}^{z_A} \mu(x,y,\xi)\mathrm{d}\xi = -\ln\left(\frac{I^{z_i}(x,y,z_A)}{I^{z_i}(x,y,z_B)}\right). \tag{1.52}$$

If we compare Eqs. 1.50 and 1.52, we immediately realize that the effect of a non-varying *PSF* (as is the case in Electron Microscopy) is equivalent to a low-pass filtration of the results with the filter given by the optical transfer function of the microscope.

1.6.4 Comparison between EM and X-ray Tomography in Fourier space

In the field of X-ray crystallography, it is well-known that the diffraction pattern that arises from an object is described in the reciprocal space (*Fourier* space) of the object by the Ewald sphere, which is the geometrical construct that defines the points that are in a constructive interference condition (Cowley, 1995).

In a similar way, this Ewald construction is also used in the field of cryo-electron microscopy, as an approximation, to analyze how projections are related to the *Fourier* transform of the sample (Wan et al, 2004). Let us take from Wan et al (2004) the equation that describes the projection in cryo-EM in *Fourier* space:

$$\begin{aligned}\hat{p}(f_x,f_y) &= \int \hat{v}_z(f_x,f_y)c_z(f_x,f_y)\mathrm{d}z \\ &= \int \hat{v}(f_x,f_y,f_z)\hat{c}(f_x,f_y,-f_z)\mathrm{d}f_z,\end{aligned} \tag{1.53}$$

where $\hat{p}$ is the 2D *Fourier* transform of the projection p, $\hat{v}_z$ is the 2D *Fourier* transform in plane (x,y) of the volume slice in the plane z, c_z is the contrast transfer function at position z, $\hat{v}$ is the 3D *Fourier* transform of the volume v and $\hat{c}$ is the 1D *Fourier* transform in the variable z of c_z.

In the case of electron microscopy, the *CTF* may be written as (Wan et al, 2004)

$$c_z = -k\cos\left(2\pi a_s z + b_s\right), \tag{1.54}$$

where $a_s = 1/2\lambda s^2$ and $b_s = -2\pi\left(C_s\lambda^3 s^4/4 - z_0\lambda s^2/2\right) - \cos^{-1} Q$ and $s = \sqrt{f_x^2+f_y^2}$, being, then, its 1D *Fourier* transform in z:

$$\hat{c}(f_x,f_y,f_z) = -\frac{k}{2}\left[e^{\mathrm{i}b_s}\delta(f_z-a_s) + e^{-\mathrm{i}b_s}\delta(f_z+a_s)\right]. \tag{1.55}$$

Therefore, Eq. 1.53 is simplified for the EM case as

$$\hat{p}(f_x,f_y) = -\frac{k}{2}\left[e^{\mathrm{i}b_s}\hat{v}(f_x,f_y,-a_s) + e^{-\mathrm{i}b_s}\hat{v}(f_x,f_y,a_s)\right]. \tag{1.56}$$

Because a_s is a quadratic function of s, Eq. 1.56 shows that in *Fourier* space, the points that contribute to the projection are placed along two parabolic surfaces instead of the expected horizontal plane crossing the coordinates' origin (figure 1.7), that is, the values experimentally measured and corresponding to the *Fourier* transform of the projection are A' and B', while the values we are mainly interested in for 3D reconstruction are those corresponding to the 3D *Fourier* transform of the specimen (A_1, A_2, B_1, B_2), with their relationships being

$$\begin{aligned} A' &= A_1 + A_2 \\ B' &= B_1 + B_2. \end{aligned}$$

Although the introduced image formation model for X-rays differs from the definition of projection for EM in Eq. 1.53 due to the combined effect of the *PSF* and the absorption, if we define

$$\begin{aligned} p'(x,y) &= I^{z_i}(x,y,z_B) - I^{z_i}(x,y,z_A) \\ v'(x,y,z) &= \mu(x,y,z') I_g^{z_i}(x,y,z_B) \exp\left(-\int_{z_B}^{z'} \mu(x,y,\xi)\mathrm{d}\xi\right), \end{aligned} \tag{1.57}$$

and substitute on Eq. 1.48, then the behavior of X-ray projections in *Fourier* space can also be analyzed by Eq. 1.53. In this case, because the EM *CTF* c_z defined for a plane z is equivalent to the *Fourier* transform of the TomoX *PSF* h, and using the definition in Eq. 1.26, we arrive at

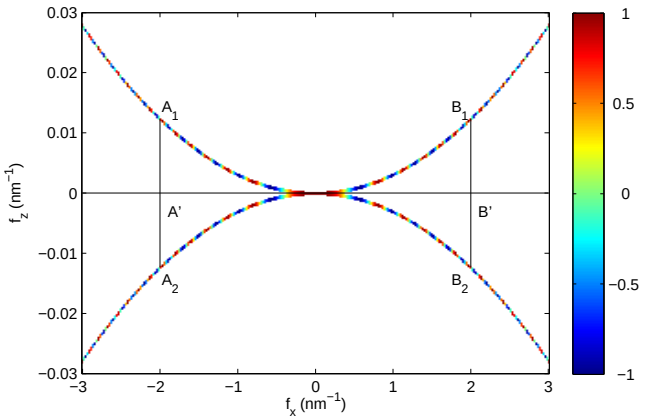

Fig. 1.7 Schematic representation in 2D *Fourier* space of a projection in an electron microscope under an illumination of 200 keV. Color lines define the *Fourier* coefficients that contribute to the projection in the integration along f_z. The A', B' points along axis f_x are the expected places for the frequential coefficients of $\hat{p}$, while they actually correspond to the summation of points $A_{1,2}, B_{1,2}$

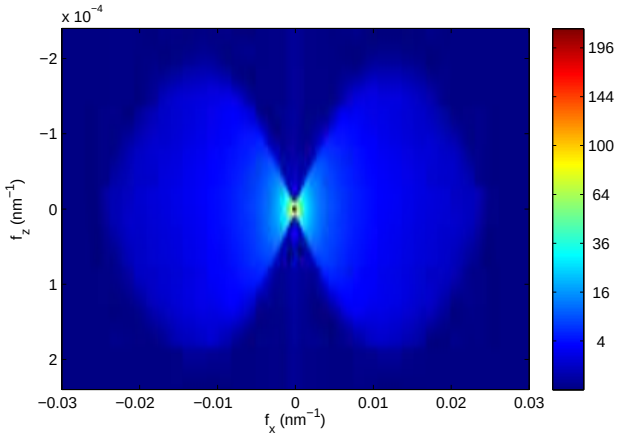

Fig. 1.8 Schematic representation in 2D *Fourier* space of a projection in an X-ray microscope. The central plane (f_x, f_z) of $\mathscr{F}_{x,y,z}\{h\}$ for the typical lens from Fig. 1.2 is shown. Note that all the coefficients on f_z along a column at frequency f_x contribute to that projection frequency f_x

$$\begin{aligned}\hat{c}(f_x, f_y, f_z) &= \mathscr{F}_z\left\{\mathscr{H}(f_x, f_y, z)\right\} = \mathscr{F}_z\left\{\mathscr{F}_{x,y}\{h(x,y,z)\}\right\} \\ &= \mathscr{F}_{x,y,z}\{h(x,y,z)\}\,, \end{aligned} \tag{1.58}$$

where $\mathscr{F}_z$ and $\mathscr{F}_{x,y,z}$ denote the *Fourier* transforms 1D in direction z and 3D in (x,y,z), respectively.

For the ideal lens case, the 3D *Fourier* transform of the *PSF* described in Eq. 1.23 has no analytical solution, although under some approximations Erhardt et al (1985) arrived at an analytical expression. In our case, from the simulated h for the typical lens shown in Fig. 1.2, we numerically calculated the 3D distribution of $\hat{c}$ and plotted it in Fig. 1.8. It is shown that there is no discrete distribution as in EM, but a continuous shape around the horizontal axis. Therefore, a frequency coefficient of a TomoX projection in plane (f_x, f_y) is obtained by the addition of many different coefficients of the *Fourier* transform of the 3D absorption distribution along f_z.

1.7 Computer simulations

We have implemented two phantoms to analyze and understand how the effect of the depth of field affects tomographic projection and 3D reconstruction in TomoX.

In the first simulation, we defined a test phantom made of fringe structures, which is depicted in Fig. 1.9. From this phantom, we can clearly detect the artifacts that are related to the characteristic TomoX depth of field. Moreover, to also have a "biologically inspired" phantom, we designed a 3D structure inspired by the *Candida albicans* reconstruction published by Uchida et al (2009), where experimental val-

ues of absorption coefficients for the different organelles were also presented (see Fig. 1.10 for details).

To simulate an X-ray microscope, we have implemented in the XMIPP image processing package (Sorzano et al, 2004; Scheres et al, 2008) a projection algorithm following the expression described by Eq. 1.48, using the 3D *PSF* of an a ideal lens with the same focal length and diameter of a Fresnel zone plate of 560 zones and an outer zone width of 40 nm (see Fig. 1.2), whose resolution and depth of field are 48.8 nm and 2.63 μm, respectively. The collection geometry is a single tilt axis with one-degree steps, with the y axis the tilt axis. According to each simulation, the data sets were generated either for a whole tilt angular range $\pm 90^\circ$ without a missing wedge or with a missing wedge between $\pm 65^\circ$.

The reconstructed tomograms from the different projections have been obtained by standard 3D software used in electron microscopy tomography, tomo3d (Agulleiro et al, 2010; Agulleiro and Fernandez, 2011; Agulleiro and Fernández, 2012), where no 3D CTF/PSF is considered.

1.7.1 Fringe test

The structure of the reference phantom is shown in Fig. 1.9(a). The structure is characterized by a set of paired fringes placed at different distances from the tilt axis y, which is on the left-hand side of the figure. The separation of the paired fringes varies along the vertical axis. The phantom has been projected under three different conditions and then reconstructed using EM-like algorithms (that is, the X-ray specific image formation process has not been taken into account). The first condition corresponds to the simplified situation in Electron Microscopy —simplified because in EM there is a *PSF*, although its dependence in z is small compared with TomoX— with a limited tilt angular range. In the two other cases, the projections have been obtained by considering the X-ray *PSF* for the whole set of projections without and with a missing wedge, respectively.

To analyze the resulting effects in the reconstruction along the z axis, we show in Fig. 1.9(b) the (x,z) planes corresponding to a fringe separation of 40 nm from: the phantom (top); the reconstructed volume from ideal EM projections with a 50° missing wedge (second); and the reconstructed volumes from X-ray projections without and with a 50° missing wedge (third and bottom rows, respectively). To quantify the effects in the tomogram due to the DOF, from the slices shown in Figs. 1.9(b) we have calculated the elongation along axis z of the reconstructed fringes and plotted in Fig. 1.9(c). Elongation is defined as half the distance between the points before and after a fringe in the z axis, where the maximum intensity of the fringe has decayed $1/\mathrm{e}$. For the ideal projection case, because there is no z-dependent *PSF*, the elongation of the fringes along the z axis is approximately constant for any radial position of the fringes (the changes basically correspond to the limited precision of the elongation measurements for very small objects). In the cases where a z-dependent

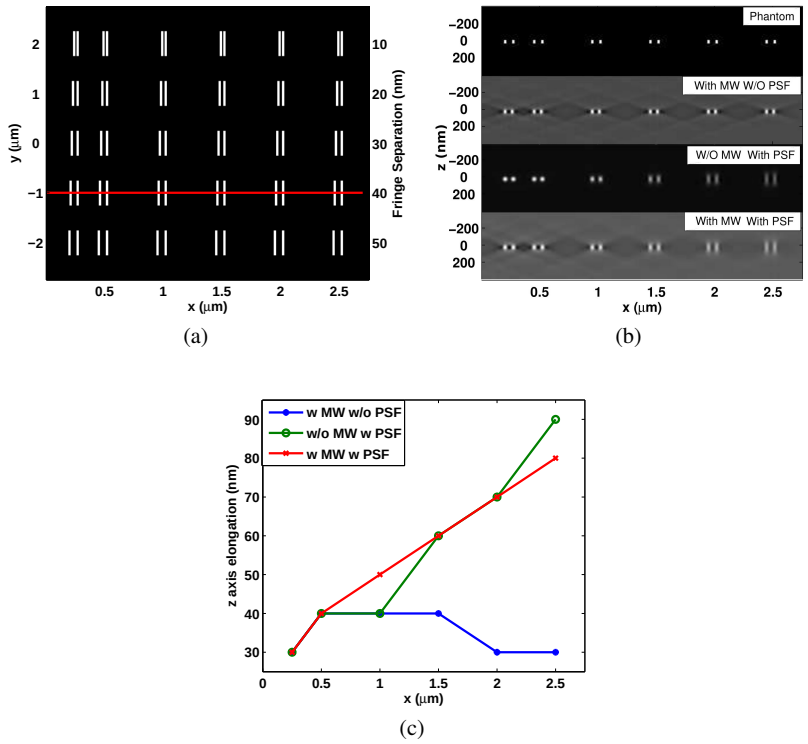

Fig. 1.9 (a) Central (x,y) slice of the fringe phantom perpendicular to the z axis (optical axis); because the phantom is symmetric along the $x = 0$ plane, only a half slice is shown (with y the tilt axis). (b) Composition of (x,z) slices from the phantom and reconstructed volumes for a fringe separation of 40 nm (red line in (a)). The images correspond to the following: phantom (top); reconstruction from ideal projections where no *PSF* has been considered for a limited tilt series with a 50° missing wedge (second); and reconstructions from X-ray projections for the cases of a complete projection set without a missing wedge (third) and with a missing wedge (bottom). (c) Comparison of the elongation along z for the different conditions shown in (b) (Reproduced with permission from Oton et al (2012))

PSF has been considered, the fringes become more elongated as they are located farther away from the tilt axis (higher x).

From Fig. 1.9(c), we note that there are no noticeable differences in elongation for the case where the X-ray *PSF* has been considered with and without a missing wedge, and the elongations in both cases are substantially greater than the elongation for the ideal EM projection case. Therefore, the effects due to the limited depth of field are much more important than those associated with missing wedge effects, which clearly illustrates the severity of the depth of field limitation.

1.7.2 Biologically inspired test

In the case of the phantom test inspired by the *Candida albicans* cell experimental 3D reconstruction (Uchida et al, 2009), a unit cell has been designed considering the yeast-like phenotype, where we have included different organelles such as a nucleus, nucleolus, mitochondria, vacuoles and lipid bodies, taking the experimentally determined linear absorption coefficients (LACs) into account to numerically evaluate the $\mu(x,y,z)$ distribution of the phantom (Fig. 1.10(a)). A pseudo cell is in the center of the phantom with the major axis lying parallel to the optical axis z, while two cell halves are placed at opposite sides of the central cell along the optical axis. The total phantom is 11 μm long, with the background value the LAC for water and the tilt axis being selected parallel to the y axis (perpendicular to the shown slices) crossing the center of the phantom.

The first set of simulations was performed supposing that the specimen embedded in water was inside a capillary, taking a full set of projections without a missing wedge. We calculated the projections ignoring the *PSF* (Eq. 1.51), which corresponds to the "simplified EM" case introduced before. For reconstruction, the data collection strategy considered a full set of projections —that is, no missing wedge— (Fig. 1.10(b)) and a limited range $\pm 65°$ as of a missing wedge effect (Fig. 1.10(c)). Both reconstructed volumes were bandpass filtered to the cut-off frequency of the Fresnel zone plate from Fig. 1.2 (48.8 nm). Fig. 1.10(b) shows the best possible reconstruction, while Fig. 1.10(c) shows the best reconstruction considering the mechanical constraints producing the missing wedge.

We then introduced the combined absorption and 3D *PSF* effects that characterize TomoX, generating the results shown in Fig. 1.11. Figure 1.11(a) shows a section along the optical axis of the 3D *PSF* used in the calculations (same plot as in Fig. 1.2), while Fig. 1.11(b) shows a section along the optical axis of the reconstruction obtained considering the full TomoX image formation model from Eq. 1.48 for the case of a data collection geometry with no missing wedge.

In all reconstructions shown in Figs. 1.10, 1.11 and 1.12, the incoming beam at $0°$ tilting angle crosses the phantom from left to right along the z direction. The most distant elements at both sides of the phantom are only in focus when the tilt angle is approximately $\pm 90°$. Moreover, the contribution of each (x,y) slice to the projection is proportional to the absorbed intensity in that slice, and the intensity decays along z. Therefore, it is clear that the contribution to the final image of slices facing the incoming beam is far greater than from those at the opposite side, producing a more detailed reconstruction of the half facing the beam. When the 3D *PSF* is considered, it introduces an inversion of contrast in the regions farther away from the center of the phantom at both sides. This effect leads to the appearance of a *double layer* artifact in the membrane-like cell feature located at the opposite end along the direction of the incoming beam at $0°$ (x axis in our reconstructions), as shown in Fig. 1.11(b), being more noticeable in the half facing the beam than in the opposite half.

To compare reconstructions from simulated projections to reconstructions from experimental tomograms, we calculated the tomograms for two different lens settings. The first simulated tomogram was calculated using the ideal lens of Fig. 1.2

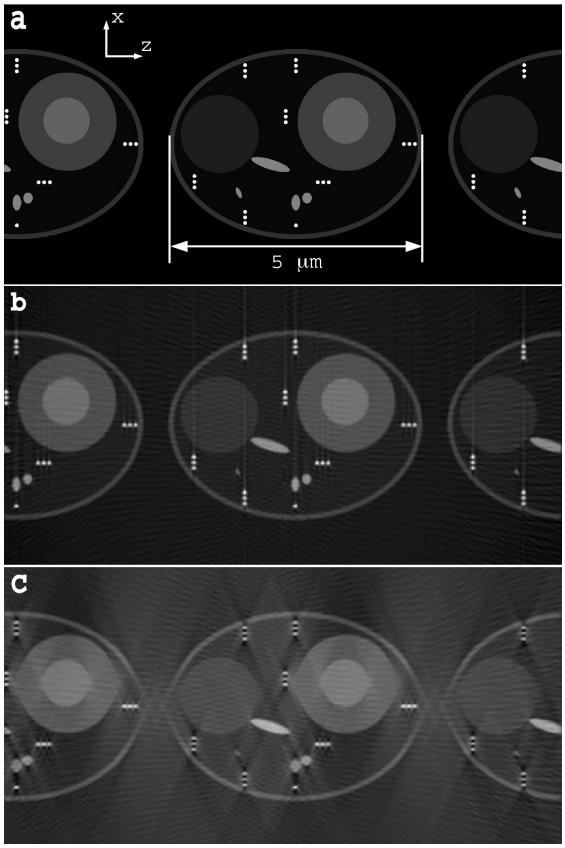

Fig. 1.10 Candida test phantom created using two copies of a "pseudo *Candida albicans*" cell placed along the optical axis z. (a) central slice of the reference phantom defined by the plane $y = 0$, (b) and (c) reconstructions from ideal projections assuming the specimen is inside a capillary with and without a 50° missing wedge, respectively, both filtered to the X-ray microscope cut-off frequency

(560 zones, 40 nm outer zone width, 44.8 μm radius, 48.8 nm resolution and 2.63 μm depth of field) for a limited tilt angular range of ±65°. The second tomogram considered projections obtained for the 3D *PSF* of an ideal lens equivalent to an FZP of 900 zones with a 45 μm radius and a 25 nm outer zone width for the same limited tilt angular range. This latter lens is one of the standard FZP settings in Bessy II, and is characterized by a focal length of 0.926 mm, a 30 nm resolution and a 1.03 μm depth of field. In Figs. 1.12(a) and (b), we show the center slice from the reconstructed volumes using lenses of 48.8 and 30 nm resolution, respectively, where we can see the combination of the artifacts due to the missing wedge and the depth of field. The central pseudo cell is well defined, except for the effects of the missing wedge on the left and right extremes of the cell membrane. The cell halves at both sides show a contrast inversion at the cell membrane produced by the limited depth of field of the lenses, which is more noticeable for the lens with the greatest resolution (Fig. 1.12(b)). Moreover, the details at the beam facing-half (left-hand side) are brighter and better defined than those at the opposite half, which is a consequence of the strong absorption.

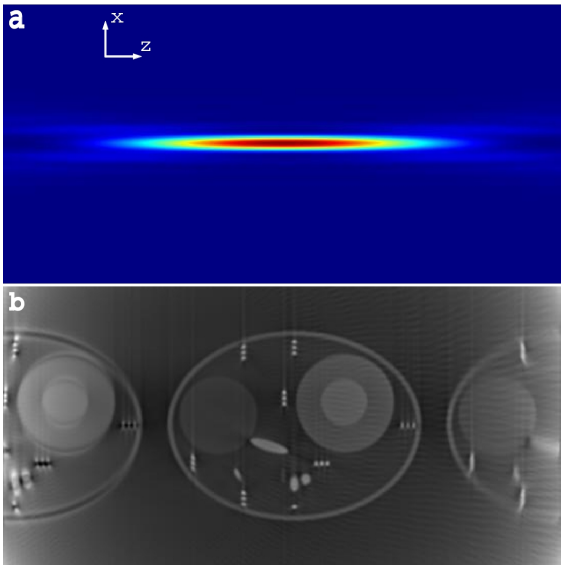

Fig. 1.11 Comparison between (a) the shape of the *PSF* in Fig. 1.2 and (b) the reconstructed center slice from X-ray projections, where the *PSF* in (a) was used. Projections were calculated assuming the specimen was inside a capillary without a missing wedge. Both images are at the same scale along the z axis, while the x axis in (a) was rescaled and reduced for the sake of visibility by a factor of 5.5

As an experimental case, we selected a reconstructed volume from a tomogram of a vaccinia virus-infected PtK2 cell on an Au-HZB2 quantifoil R 2/2 grid, which was acquired in X-ray microscope beamline U41 of Bessy II using an FZP with the same parameters as the 48.8 nm resolution lens used in the previous simulations. An (x,z) plane of the experimental reconstruction corresponding to a section of the PtK2 cell nucleus is shown in Fig. 1.12(c) at the same scale as the reconstructions shown in Figs. 1.12(a) and (b). It is clear that the central part of the tomogram, corresponding to approximately half the total depth, shows a well-delineated nuclear membrane, where the sections on the far left and far right (along the optical axis) are blurred due to the missing wedge. Past this central part, the features are far less defined. There is an invagination of the cell on the top right corner whose membrane is blurred and even contrast inverted. We also note that the features on the left-hand side of Fig. 1.12(c) are brighter than on the right-hand side. If we compare these characteristics to those shown by the simulation in Fig. 1.12(a), we note similar effects. Indeed, the "central" pseudo cell is generally well reconstructed, while the cell halves on the left and right sides are more blurred. Moreover, the half pseudo cell on the left-hand side of Fig. 1.12(c) is brighter than the corresponding one on the right-hand side. These results confirm a good agreement between the reconstructions from experimental projections and the reconstructions from the simulated projections using our proposed image formation model.

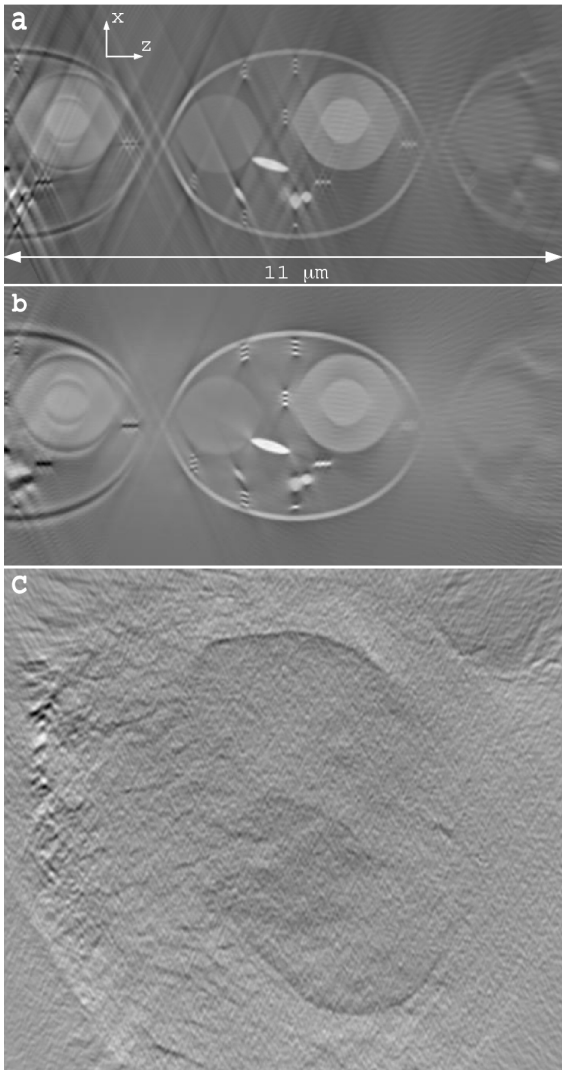

Fig. 1.12 Comparison of reconstructions from simulated and experimental tomograms with a tilt angular range of ±65°. Central slices of the reconstruction from simulated projections using (a) the 48.8 nm resolution lens (2.63 μm DOF) shown in Fig. 1.2 and (b) a 30 nm resolution lens (1.03 μm DOF). (c) reconstruction of a vaccinia virus-infected PtK2 cell from experimental projections using the 48.8-nm-resolution lens in the U41 beamline at Bessy II

1.8 Conclusions

In this chapter, we proposed an image formation model based on the approximation of incoherent illumination. This model allows a better understanding of the imaging process in TomoX of thick specimens and will be, in a future study, modified to include the coherent illumination case. Within its limitations, this model is a first step toward the development of reconstruction algorithms specific to TomoX.

Compared with EM tomography and analyzing the situation in *Fourier* space, the first obvious difference is that while a projection coefficient in EM is related to

only two points (voxels) in the specimen, in soft X-rays a projection coefficient is related to a whole line of voxels. This effect is a consequence of the different optical processes governing the image formation in both types of microscopes. Therefore, reconstruction methods used in EM that correct the position of *Fourier* coefficients along the parabolic surface defined by EM CTFs cannot be applied in the X-ray tomography field.

The analysis of our simulations indicates that the deformations (elongations) caused by the limited depth of field of TomoX are much more important than the missing wedge-related deformations. However, they mainly happen, as expected, outside the depth of field of X-ray lenses. Furthermore, we note that the part of the specimen facing the X-ray beam is brighter than the part farther away. This result is a consequence of the exponential decay in the number of absorbed photons. Finally, we quantitatively compared simulations with experimental observations and found a good correlation, which indicates that the image formation model described in this chapter represents an important step forward in the quantitative understanding of TomoX images.

As a closing remark, we note that most TomoX reconstructions are currently performed with the low-resolution Fresnel zone plate. However, our natural quest for higher resolution reconstructions will require the use of Fresnel zone plates with higher resolution and, concomitantly, smaller depth of field, which will lead to an increase of artifacts in 3D reconstructions —as very clearly illustrated in Fig. 1.12(c)— unless new TomoX-specific 3D reconstruction methods are developed.

Acknowledgements The authors would like to acknowledge financial support from the Spanish Ministry of Economy and Competitiveness (MEC) through Grants AIC-A-2011-0638 and BIO2010-16566; the Comunidad de Madrid through grant CAM(S2010/BMD-2305); and the European Community's Seventh Framework Programme (FP7/2007-2013) under BioStruct-X (CAP-INFRAS/1376) and NSF Grant DMS-1114901. C.O.S. Sorzano is a recipient of a *Ramón y Cajal* fellowship financed by the European Social Fund and MEC. Joaquín Otón is supported by a *Juan de la Cierva* fellowship from MEC with reference JCI-2010-07594.

Appendix

In this appendix, we demonstrate a more detailed derivation of Eq. 1.43 from Eq. 1.42. We begin from the expression of the electric field in plane z given in Eq. 1.39, described as a convolution following the general guide-lines provided by Goodman (1996) Section 6.1.3.

$$
\begin{aligned}
I^{z_i}(x,y,z'+\Delta z') &= \left\langle U^{z_i}(x,y,z'+\Delta z')U^{z_i*}(x,y,z'+\Delta z')\right\rangle \\
&= \Big\langle \iiiint U_g^{z_i}(\xi,\eta,z'+\Delta z')\tilde{h}(x-\xi,y-\eta,z'+\Delta z')\mathrm{d}\xi\,\mathrm{d}\eta \\
&\quad U_g^{z_i*}(\xi',\eta',z'+\Delta z')\tilde{h}^*(x-\xi',y-\eta',z'+\Delta z')\mathrm{d}\xi'\mathrm{d}\eta'\Big\rangle \\
&= \Big\langle \iiiint \left(1-\tilde{\mu}^R(\xi,\eta,z')\Delta z'-\mathrm{i}\tilde{\mu}^I(\xi,\eta,z')\Delta z'\right) \\
&\quad U_g^{z_i}(\xi,\eta,z')\tilde{h}(x-\xi,y-\eta,z'+\Delta z') \\
&\quad \left(1-\tilde{\mu}^R(\xi',\eta',z')\Delta z'+\mathrm{i}\tilde{\mu}^I(\xi',\eta',z')\Delta z'\right) \\
&\quad U_g^{z_i*}(\xi',\eta',z')\tilde{h}^*(x-\xi',y-\eta',z'+\Delta z') \\
&\quad \mathrm{d}\xi\,\mathrm{d}\eta\,\mathrm{d}\xi'\mathrm{d}\eta'\Big\rangle \\
&= \Big\langle \iiiint \left(1-\tilde{\mu}^R(\xi,\eta,z')\Delta z'-\mathrm{i}\tilde{\mu}^I(\xi,\eta,z')\Delta z'\right) \\
&\quad \left(1-\tilde{\mu}^R(\xi',\eta',z')\Delta z'+\mathrm{i}\tilde{\mu}^I(\xi',\eta',z')\Delta z'\right) \\
&\quad U_g^{z_i}(\xi,\eta,z')U_g^{z_i*}(\xi',\eta',z') \\
&\quad \tilde{h}(x-\xi,y-\eta,z'+\Delta z')\tilde{h}^*(x-\xi',y-\eta',z'+\Delta z') \\
&\quad \mathrm{d}\xi\,\mathrm{d}\eta\,\mathrm{d}\xi'\mathrm{d}\eta'\Big\rangle
\end{aligned}
\tag{1.59}
$$

To calculate the image intensity, we must time average the instantaneous intensity. Because the detector integration time is long compared with the period of the wave, and because of the case of totally incoherent illumination (Goodman (1996) Eqs. 6.7 to 6.15)

$$
\left\langle U_g^{z_i}(\xi,\eta,z')U_g^{z_i*}(\xi',\eta',z')\right\rangle \propto I_g^{z_i}(\xi,\eta,z')\delta(\xi-\xi',\eta-\eta'),
\tag{1.60}
$$

then Eq. 1.59 simplifies to

$$
\begin{aligned}
I^{z_i}(x,y,z'+\Delta z') &= \iint \left(1-\tilde{\mu}^R(\xi,\eta,z')\Delta z'-\mathrm{i}\tilde{\mu}^I(\xi,\eta,z')\Delta z'\right) \\
&\quad \left(1-\tilde{\mu}^R(\xi,\eta,z')\Delta z'+\mathrm{i}\tilde{\mu}^I(\xi,\eta,z')\Delta z'\right) I_g^{z_i}(\xi,\eta,z') \\
&\quad \tilde{h}(x-\xi,y-\eta,z'+\Delta z')\tilde{h}^*(x-\xi,y-\eta,z'+\Delta z')\mathrm{d}\xi\,\mathrm{d}\eta \\
&= \iint \Big(1-2\tilde{\mu}^R(\xi,\eta,z')\Delta z'+ \\
&\quad \left[\tilde{\mu}^R(\xi,\eta,z')^2+\tilde{\mu}^I(\xi,\eta,z')^2\right]\left(\Delta z'\right)^2\Big) \\
&\quad I_g^{z_i}(\xi,\eta,z')\left|\tilde{h}(x-\xi,y-\eta,z'+\Delta z')\right|^2\mathrm{d}\xi\,\mathrm{d}\eta \\
&= \left[\left(1-2\tilde{\mu}^R(\xi,\eta,z')\Delta z'+O(\Delta z'^2)\right)I_g^{z_i}(x,y,z')\right]\underset{x,y}{\otimes} \\
&\quad \left|\tilde{h}(x,y,z'+\Delta z')\right|^2.
\end{aligned}
\tag{1.61}
$$

References

Agulleiro J, Fernandez J (2011) Fast tomographic reconstruction on multicore computers. Bioinformatics 27(4):582–583, DOI 10.1093/bioinformatics/btq692, URL http://bioinformatics.oxfordjournals.org/content/27/4/582.short

Agulleiro JI, Fernández JJ (2012) Evaluation of a multicore-optimized implementation for tomographic reconstruction. PloS one 7(11):e48,261, DOI 10.1371/journal.pone.0048261, URL http://dx.plos.org/10.1371/journal.pone.0048261

Agulleiro JI, Garzón EM, García I, Fernández JJ (2010) Vectorization with SIMD extensions speeds up reconstruction in electron tomography. Journal of structural biology 170(3):570–5, DOI 10.1016/j.jsb.2010.01.008, URL http://www.ncbi.nlm.nih.gov/pubmed/20085820

Attwood D (2007) Soft X-Rays and Extreme Ultraviolet Radiation: Principles and Applications, 1st edn. Cambridge University Press, New York, NY, USA

Bertilson M, von Hofsten O, Vogt U, Holmberg A, Christakou AE, Hertz HM (2011) Laboratory soft-x-ray microscope for cryotomography of biological specimens. Optics letters 36(14):2728–30, DOI 10.1364/OL.36.002728, URL http://www.ncbi.nlm.nih.gov/pubmed/21765523 http://ol.osa.org/abstract.cfm?URI=ol-36-14-2728

Born M, Wolf E (1999) Principles of Optics: Electromagnetic Theory of Propagation, Interference and Diffraction of Light, 7th edn. Cambridge University Press

Carrascosa JL, Chichón FJ, Pereiro E, Rodríguez MJ, Fernández JJ, Esteban M, Heim S, Guttmann P, Schneider G (2009) Cryo-X-ray tomography of vaccinia virus membranes and inner compartments. Journal of structural biology 168(2):234–9, DOI 10.1016/j.jsb.2009.07.009, URL http://www.ncbi.nlm.nih.gov/pubmed/19616103

Chapman HN, Nugent Ka (2010) Coherent lensless X-ray imaging. Nature Photonics 4(12):833–839, DOI 10.1038/nphoton.2010.240, URL http://www.nature.com/doifinder/10.1038/nphoton.2010.240

Chichón FJ, Rodríguez MJ, Pereiro E, Chiappi M, Perdiguero B, Guttmann P, Werner S, Rehbein S, Schneider G, Esteban M, Carrascosa JL (2012) Cryo X-ray nano-tomography of vaccinia virus infected cells. Journal of structural biology 177(2):202–11, DOI 10.1016/j.jsb.2011.12.001, URL http://www.ncbi.nlm.nih.gov/pubmed/22178221

Cowley J (1995) Diffraction physics, 3rd edn. Elsevier

Erhardt a, Zinser G, Komitowski D, Bille J (1985) Reconstructing 3-D light-microscopic images by digital image processing. Applied optics 24(2):194, URL http://www.ncbi.nlm.nih.gov/pubmed/18216925

Folland GB (1992) Fourier analysis and its applications. Wadsworth & Brooks/Cole Advanced Books & Software, Pacific Grove Calif.

Frank J (2006) Three Dimensional Electron Microscopy of Macromolecular Assemblies. Oxford University Press, New York

Frank J, Radermacher M, Penczek P, Zhu J, Li Y, Ladjadj M, Leith A (1996) SPIDER and WEB: processing and visualization of images in 3D electron microscopy and related fields. J Struct Biol 116:190–199

Goodman JW (1996) Introduction to Fourier Optics. McGraw-Hill, New York

Gros ML, McDermott G, Larabell C (2005) X-ray tomography of whole cells. Current opinion in structural ... 15:593–600, URL http://www.sciencedirect.com/science/article/pii/S0959440X05001569

Gu W, Etkin L, Gros ML, Larabell C (2007) X-ray tomography of Schizosaccharomyces pombe. Differentiation 75:529–535, URL http://onlinelibrary.wiley.com/doi/10.1111/j.1432-0436.2007.00180.x/full

Hanssen E, Knoechel C (2012) Soft X-ray microscopy analysis of cell volume and hemoglobin content in erythrocytes infected with asexual and sexual stages of Plasmodium falciparum. Journal of structural ... URL http://www.sciencedirect.com/science/article/pii/S1047847711002589

Heymann JB, Cardone G, Winkler DC, Steven AC (2008) Computational resources for cryo-electron tomography in Bsoft. Journal of structural biology 161(3):232–42, DOI 10.1016/j.jsb.2007.08.002

Howells M, Jacobsen C, Warwick T, Bos A (2007) Principles and applications of zone plate X-ray microscopes. In: Science in Microscopy, vol 1984, {P.W} hawk edn, pp 835–926, URL http://www.springerlink.com/index/W76K0246K3HG7W26.pdf

Jacobson RE, Ray SF, Attridge GG, Axford NR (2001) Manual of Photography: Photographic and Digital Imaging, ninth edn. Focal Press, London, URL http://dl.acm.org/citation.cfm?id=558275

Kirz J, Jacobsen C, Howells M (1995) Soft X-ray microscopes and their biological applications. Q Rev Biophys 28:33–130

Kremer JR, Mastronarde DN, McIntosh JR (1996) Computer visualization of three-dimensional image data using IMOD. J Struct Biol 116:71–76

Larabell C (2004) X-ray tomography generates 3-D reconstructions of the yeast, Saccharomyces cerevisiae, at 60-nm resolution. Molecular biology of the cell 15(March):957–962, DOI 10.1091/mbc.E03, URL http://www.molbiolcell.org/content/15/3/957.short

Legall H, Blobel G, Stiel H, Sandner W, Seim C, Takman P, Martz DH, Selin M, Vogt U, Hertz HM, Esser D, Sipma H, Luttmann J, Höfer M, Hoffmann HD, Yulin S, Feigl T, Rehbein S, Guttmann P, Schneider G, Wiesemann U, Wirtz M, Diete W (2012) Compact x-ray microscope for the water window based on a high brightness laser plasma source. Optics express 20(16):18,362–9, URL http://www.ncbi.nlm.nih.gov/pubmed/23038387

Martínez-Corral M, Zapata-Rodríguez C (1998) Effective Fresnel-number concept for evaluating the relative focal shift in focused beams. JOSA A 15(2):449–455, URL http://www.opticsinfobase.org/abstract.cfm?id=1405

McDermott G, Le Gros Ma, Larabell Ca (2012) Visualizing cell architecture and molecular location using soft x-ray tomography and correlated cryo-light microscopy. Annual review of physical chem-

istry 63:225–39, DOI 10.1146/annurev-physchem-032511-143818, URL http://www.ncbi.nlm.nih.gov/pubmed/22242730

Mendoza-Yero O, Minguez-Vega G, Navarro R, Lancis J, Climent V (2010) PSF analysis of nanometric Fresnel zone plates. In: Proceeding of the EOS Topical Meeting on Diffractive Optics, Koli, Finland

Mielenz KD (1999) On the Diffraction Limit for Lensless Imaging. Journal of Research of NIST 104(5):479–485

Nelson J, Huang X, Steinbrener J, Shapiro D, Kirz J, Marchesini S, Neiman AM, Turner JJ, Jacobsen C (2010) High-resolution x-ray diffraction microscopy of specifically labeled yeast cells. Proceedings of the National Academy of Sciences of the United States of America 107(16):7235–9, DOI 10.1073/pnas.0910874107

Oton J, Sorzano COS, Pereiro E, Cuenca-Alba J, Navarro R, Carazo JM, Marabini R (2012) Image formation in cellular X-ray microscopy. Journal of structural biology 178(1):29–37, DOI 10.1016/j.jsb.2012.01.006, URL http://dx.doi.org/10.1016/j.jsb.2012.01.006

Parkinson D, McDermott G (2008) Quantitative 3-D imaging of eukaryotic cells using soft X-ray tomography. Journal of structural ... 162:380–386, URL http://journals.cambridge.org/production/action/cjoGetFulltext?fulltextid=1945896

Rehbein S, Heim S, Guttmann P, Werner S (2009) Ultrahigh-resolution soft-X-ray microscopy with zone plates in high orders of diffraction. Physical review letters 110801(September):1–4, DOI 10.1103/PhysRevLett.103.110801, URL http://link.aps.org/doi/10.1103/PhysRevLett.103.110801

Sakdinawat A, Attwood D (2010) Nanoscale X-ray imaging. Nature Photonics 4(12):840–848, DOI 10.1038/nphoton.2010.267, URL http://www.nature.com/doifinder/10.1038/nphoton.2010.267

Scheres SHW, Núñez Ramírez R, Sorzano COS, Carazo JM, Marabini R (2008) Image processing for electron microscopy single-particle analysis using XMIPP. Nature protocols 3(6):977–90, DOI 10.1038/nprot.2008.62, URL http://dx.doi.org/10.1038/nprot.2008.62

Schneider G (1998) Cryo X-ray microscopy with high spatial resolution in amplitude and phase contrast. Ultramicroscopy 75(2):85–104, URL http://www.ncbi.nlm.nih.gov/pubmed/9836467

Sorzano COS, Marabini R, Velázquez-Muriel J, Bilbao-Castro JR, Scheres SHW, Carazo JM, Pascual-Montano A (2004) XMIPP: a new generation of an open-source image processing package for electron microscopy. J of Struct Biol 148(2):194–204, DOI 10.1016/j.jsb.2004.06.006, URL http://www.ncbi.nlm.nih.gov/pubmed/15477099

Sypek M, Makowski M, Kolodziejczyk A, Navarro R (2010) Calculations of PSF functions for X-ray zone plates with high number of zones. In: Proceeding of the EOS Topical Meeting on Diffractive Optics, Koli, Finland

Thieme J, Schneider G, Knochel C (2003) X-ray tomography of a microhabitat of bacteria and other soil colloids with sub-100 nm resolution. Micron 34:339–344

Uchida M, McDermott G, Wetzler M, Le Gros Ma, Myllys M, Knoechel C, Barron AE, Larabell Ca (2009) Soft X-ray tomography of phenotypic switching and the cellular response to antifungal peptoids in Candida albicans. Proceedings of the

National Academy of Sciences of the United States of America 106(46):19,375–80, DOI 10.1073/pnas.0906145106

Wan Y, Chiu W, Zhou Z (2004) Full contrast transfer function correction in 3D cryo-EM reconstruction. Communications, Circuits and . . . 2

Weiss D, Schneider G, Niemann B, Guttmann P, Rudolph D, Schmahl G (2000) Computed tomography of cryogenic biological specimens based on X-ray microscopic images. Ultramicroscopy 84(3-4):185–197, URL http://www.ncbi.nlm.nih.gov/pubmed/10945329 http://www.sciencedirect.com/science/article/pii/S0304399100000346

Wolter H (1952) Spiegelsysteme streifenden Einfalls als abbildende Optiken für Röntgenstrahlen. Annalen der Physik 445:94–114, DOI 10.1002/andp.19524450108

Index